Improving Localization of Planetary Rovers with Absolute Bearing by Continuously Tracking the Sun

Curtis Boirum

CMU-RI-TR-16-01

January 7, 2015

The Robotics Institute
Carnegie Mellon University
Pittsburgh, Pennsylvania 15213

Abstract

Achieving meaningful exploration and discovery in our universe pivots on knowing where we are as we navigate the unknown. In many terrestrial cases this problem - the localization problem - has been remedied by precise a priori mapping of environments and developing advanced infrastructure such as global positioning satellites (GPS). However, extraterrestrial surface exploration robots do not have these absolute measurement tools at their disposal and achieving precise localization is still a limiting and time consuming problem. Even though it is essential to modern spacecraft and naval vessels, observing the sun and stars as absolute orientation references had, until now, not yet been fully exploited in real-time on surface rovers. Sun compassing has seen only limited, intermittent use on the moon and Mars for roving despite the potential for vastly increasing explorative capability. To this end, this work asserts that using a visual sun compass as a navigational aid to continuously determine absolute bearing substantially improves the ability of planetary rovers to navigate and localize, and supports this claim through the presentation of experimental results from the development and field testing of a high rate 187° field of view visual sun compass.

Acknowledgments

There are no words, written or spoken, that will ever be able to fully convey my gratitude and appreciation for everything my wonderful wife Kristie has done, put up with, lived through, sacrificed, and endured so that I could pursue my dream and become who I was born to be. Our journey to the far away land of Pittsburgh with our 6 month old began an adventure that has been nothing if not challenging. I could never have hoped for someone whose trust, moral fiber, strength, resolve, and love match hers – sometimes you just get lucky. All I can say is thank you.

Thank you Red, for your patience and understanding, for your attention and feedback, for your motivation and comradery, for sharing your perspective, for your friendship, trust, and for everything.

Thank you Chuck for your tireless hours in the field and on campus – always with a smile to help at any hour for any reason.

Thank you Devin and Jenna Suiter and Julia Teresa for your always cheerful and lifesaving help.

Thank you Dan and Eugene for always diving in deep with me at a moment's notice and never looking back.

I also owe a great debt of gratitude to my thesis committee members Dr. George Kantor and Heather Jones for your extraordinary patience and insight.

Table of Contents

1. Introduction

Robotic exploration offers humanity the potential to venture into and examine every crater, cave, valley and plain in our solar system with much less risk, cost, and a shorter time frame than if done with human explorers. The recent explosion in miniaturization of powerful computing and sensing technology promises to make the next generation of robots smaller, more numerous, and far more capable than ever before. The material and scientific rewards humanity may reap by remotely roving these vast unknown surfaces may seem endless, but they are merely vague dreams and half promises without the reliable and precise ability to navigate.

Well known and well behaved environments have become familiar places for robots. Vacuums in living rooms, stock retrieval machines in warehouses, and cars on test tracks are examples where robotic vehicles are functioning with relative ease and reliability. However, take away the artificial beacons, GPS satellites, straight hallways, smooth floors and highly detailed maps - and the vision of speed, self-driving, and time saving artificial intelligent becomes a landscape of slow, risk averse, tedious, human remote operation. This is because automated navigation and planning can only occur when there is high enough certainty of absolute position within an environment that is also known with enough certainty. Predictable and geometrically well-defined environments (such as hallways and roads) offer enough frequent and easily identifiable landmarks, edges, corners, etc. that today's localization algorithms can quickly make estimations with confidence (Thrun 2002; Borenstein et al. 1997; Li et al. 2006; Bapna et al. 1998).

Fully natural environments typically do not offer unique features of sufficiently recognizable geometry for robots to match their surroundings to an orbital imagery map automatically. This is possible, and currently utilized, but is processor intensive, and requires a tall mast (>0.5m), high resolution ground imagery, and flat terrain or onboard dense 3D reconstruction (Sheshadri et al. 2012). This necessitates a large amount of manual intervention by operators to plan out carefully tailored paths. The higher precision a robot can estimate its relative location to a known starting point, the less frequently absolute position registrations need to be performed. This relative pose estimation is most commonly performed by the technique of dead reckoning, where a vehicle integrates its own measured rates of movement over time to predict a change in position. Typically, a forward change in distance estimate is combined with a change in heading estimate to calculate a change in position. All of these position change estimates are combined into a global position estimate (Betke & Gurvits 1997; Borenstein & Feng 1996).

Modern spacecraft, aircraft, guided weapons, ships, and other vehicles use dead reckoning as a first step in localization. Dead reckoning is ubiquitous and convenient because it only requires the measurement of internal relative changes in state. However, with dead reckoning alone, an unbounded position error accumulates over time because each relative measurement contains a finite amount of additive random error. Even with the most precise sensors available, the position estimate will eventually diverge and become unusable without timely correction from absolute external measurements (such as map landmark registrations, GPS updates, star/sun tracking, etc.).

The most influential and unfortunately numerically unstable measurement therein is incremental change in heading (or more generally, direction of travel). This is typically measured using a gyroscope, wheel steering angles, or difference in right and left wheel travel for differential drive robots. Compared to errors in incremental position estimates, relatively small errors in heading estimates cause disproportionately large position errors. Additionally, the random drift error inherent in incremental heading measurements cannot be eliminated by systematic calibration or characterization. Without some form of periodic absolute heading measurement – whether inferred from landmark observations, a compass, or other means – the dead reckoning estimate quickly diverges. Furthermore, most extraterrestrial bodies lack a useable magnetic field, and none have GPS. Periodic position updates are performed using satellite imaging in some cases, but this method is highly constraining and may not always be available or practical. (Borenstein et al. 1996; Lamon 2008; Li et al. 2006; Li et al. 2005; Maimone et al. 2007; Ali et al. 2005)

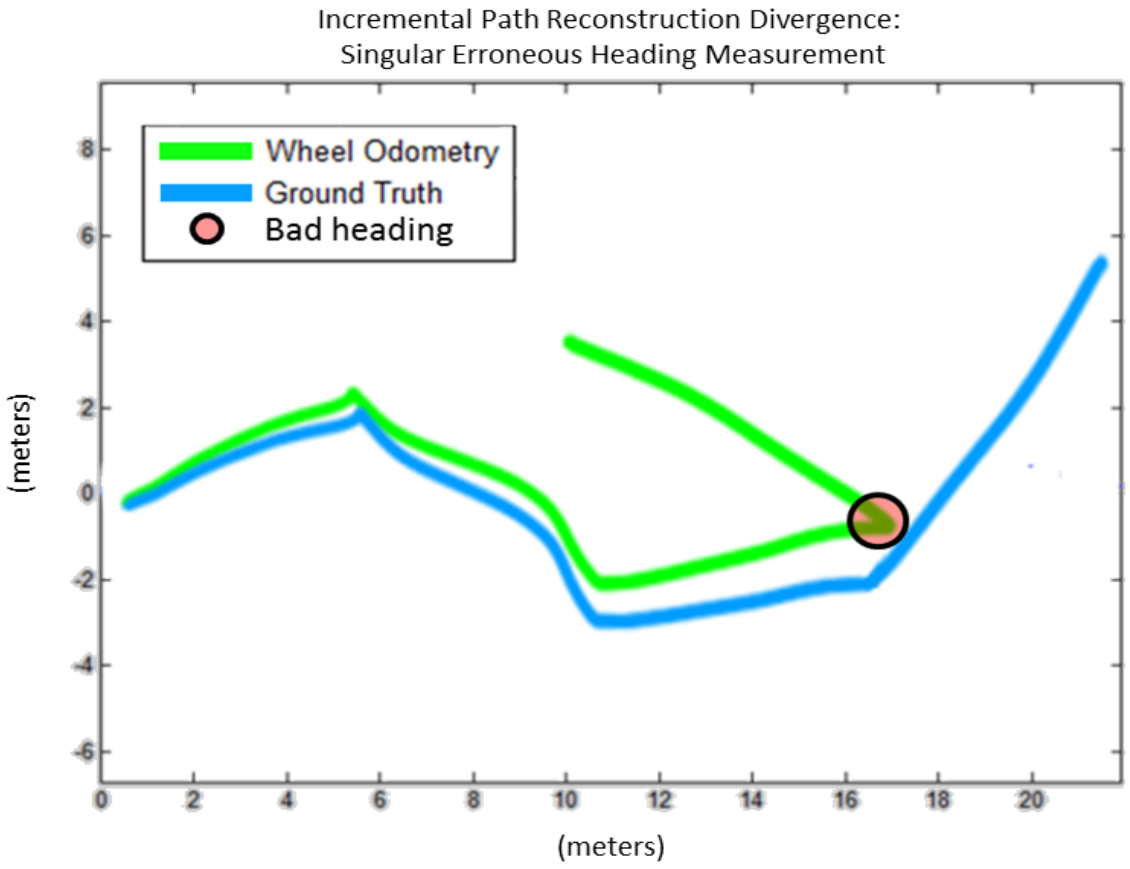

Figure 1: Singular heading error corrupts incremental dead reckoning data

The sun is perhaps the most dependable and accurate source of absolute heading reference in the solar system. Modern spacecraft use the sun as a first reference before performing fine attitude determination by star tracking. Bats have been shown to use the sun to calibrate their internal direction finding mechanism daily at sunset. Many insects including bees and ants have also been shown to use the sun as an absolute direction reference. From 1850 until at least 1973, manually operated sun compasses were a preferred method (over magnetic) of heading reference for official United States land surveys (United_States_Department_of_the_Interior 1973). The United States Naval Academy reinstated required training of celestial navigation in 2015 due to the realized risk of hacking/disabling GPS satellites.

This research solves many of the biggest problems faced by sun compass researchers in the past and shows that a novel high rate 187° field of view visual sun compass combined with only wheel odometry can achieve as good or better localization results as Inertial Measurement Units (IMUs), visual odometry, and other techniques in operating conditions significant to planetary exploration. A novel night field test with an artificial sun demonstrates the sun compass' performance when cloud cover is not an issue, and highlights its potential for use in lunar polar exploration.

2. Priors

The first time a sun compass was used extra-terrestrially was on the moon by Apollo 15 astronaut, Commander David Scott, during the initial "Stand-Up EVA" after landing. The sun compass was later used to assist navigating the Lunar Roving Vehicle. The device was manual and only used intermittently as needed, but Scott recalled that "It was a great get-me-home device," in reference to its essential navigation role (Jones 1996). The paper card sun compass can be seen in the figure below.

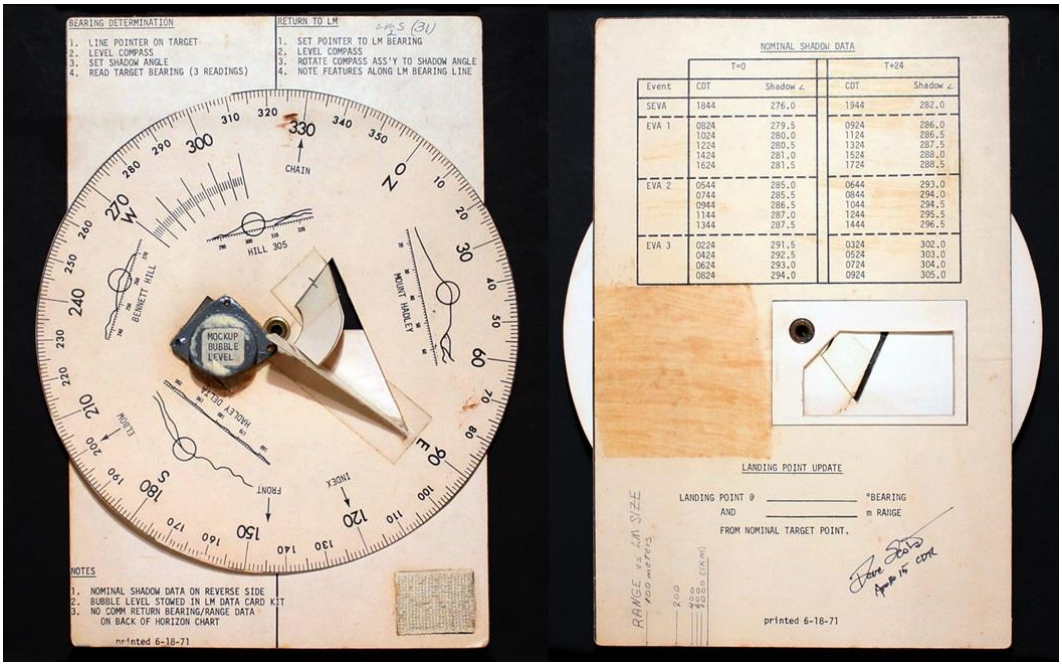

Figure 2: Manual sun compass used on Apollo 15.

Cozman & Krotkov (1995) appear to be the first to combine marine navigation, satellite attitude determination and computer vision techniques to observe the sun for the purpose of localizing a robot. The primary difficulty was maintaining track of the sun with the narrow field of view camera, in contrast to the 187° fisheye lens used in this research. Volpe (1999) performed a one kilometer length field test in desert terrain using a fisheye lens analog sun sensor to measure absolute heading aboard the 15.5kg Rocky 7 rover. Volpe found position error was linearly related to traverse length when using the sun compass, and quadratic when integrating a heading rate gyroscope, which is in agreement with this paper's findings. Difficulties with wide field of view lens calibration caused errors in heading determination. The current research utilized recent advances in wide angle lens calibration to nullify this problem.

Trebi-Ollennu et al. (2001) developed a narrow lens camera based system and investigated error propagation and sensitivities using the FIDO rover. Sun detection was performed by image brightness threshold, binary growth and erosion pixel operations to reduce noise, and segmented regions scrutinized by circularity checking. Neutral density filters were used to reduce glare in the image, but did not attenuate noise from reflections and proximal cloud scattering. The current research tested the sun sensor at night with an artificial sun, which eliminated sun detection inaccuracy caused by cloud scattering. The effect of reflections and other noise sources was reduced by capturing images with a variable and very short exposure time instead of the neutral density filter approach by previous researchers. Noise was further reduced by performing Otsu thresholding instead of brightness only thresholding. Circularity

checking was not necessary using the new method, and combined with the short image exposure time, allows for higher detection sensitivity to identify the sun even when highly occluded and while the rover is moving over rough terrain.

Baumgartner et al. (2001) and Huntsberger et al. (2002) field tested a camera based sun sensor on the FIDO rover over traverses in the 10-130m range. The sun compass was integrated with the entire localization system using an Extended Kahlman Filter. Results were again promising, but the sun compass heading was only used at the beginning and end of traverses to correct for gyroscopic bias. Long distance route determination accuracy for the 135m FIDO trek was not reported because of the failure of the GPS ground truth system. The current research used a highly reliable robotic total survey station to ensure accurate ground truth for long and short distances. The strategy of intermittent sun sensing using these algorithms was then implemented on the NASA Mars Exploration Rovers, Spirit and Opportunity. However, the planned dedicated sun sensors were eliminated to reduce costs and the MERs instead detected the sun's position using their general-purpose panoramic cameras. Images of the sun were taken with a 0.5 second exposure, necessitating a pause in traverse for every measurement (Eisenman et al. 2002). From 2004 to 2007, the MERs only measured absolute heading by sun slightly over 100 times (Maimone et al. 2007).

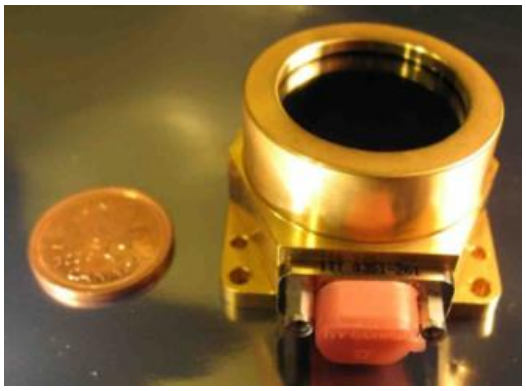

Figure 3: Sinclair Interplanetary SS-411 digital sun sensor (Lambert 2010)

Lambert, et. al, (2010) achieved a mean route determination error of 6% of distance traveled using a Sinclair Interplanetary SS-411 digital sun sensor in concert with an inclinometer and stereo pair visual odometry on a series of twenty-three challenging 100-500m terrain traverses that totaled a 10km closed loop. Their results showed on average for thirteen 400m traverses a roughly 20% decrease in route determination error when the sun compass was used with visual odometry (instead of visual odometry alone). The current research performs a single trek of 300m in length in similar terrain and achieved 4.6% error without visual odometry – using only wheel odometry.

3. Technical Approach

The technical approach for exhibiting the merits of sun-sensing for improving localization of planetary rovers is to compare error in route determination with and without sun compass absolute heading. The goal of improving localization will be met if the position error of route determination using the sun compass is substantially lower than that of other relevant methods. The other relevant methods used in this work are wheel odometry integration, and Inertial Measurement Unit (IMU) heading integration with odometry integration. Results from other methods in the literature including visual odometry and Kalman filtering are also compared. To generate the necessary data for route determination a novel sun compass is developed on an existing lunar rover prototype and field tested in a novel 300m outdoor traverse over lunar like terrain with an artificial sun at night to preclude the troublesome errors caused by cloud scattering of the sun during the day. The sun compass continuously takes images of the artificial sun at 1Hz, ensuring no significant gaps in sun tracking by using a 187° fisheye lens. The sun is detected in these images using computer vision, and lens distortion is corrected by using appropriate calibration. Finally, the approach to finding heading is to convert sun position in image to a relative sun bearing, compensate for rover tilt as estimated by onboard sensors in order to find the true sun bearing, and use an ephemeris to find true absolute heading given the true sun bearing, date and time, and approximate latitude and longitude.

3.1. Route Determination

The ultimate merit of the sun compass is evaluated by comparing the various route determinations of a traverse as made with and without sun compass data. A very simple two dimensional relative pose estimation algorithm was used to cumulatively generate a driven trajectory estimate. In all route reconstruction cases, wheel odometry (C_L and C_R) is used to determine the distance traversed. Each case uses a different method to estimate heading (θ). The figure below shows the simplified vehicle model on the left, and the actual rover planform on the right.

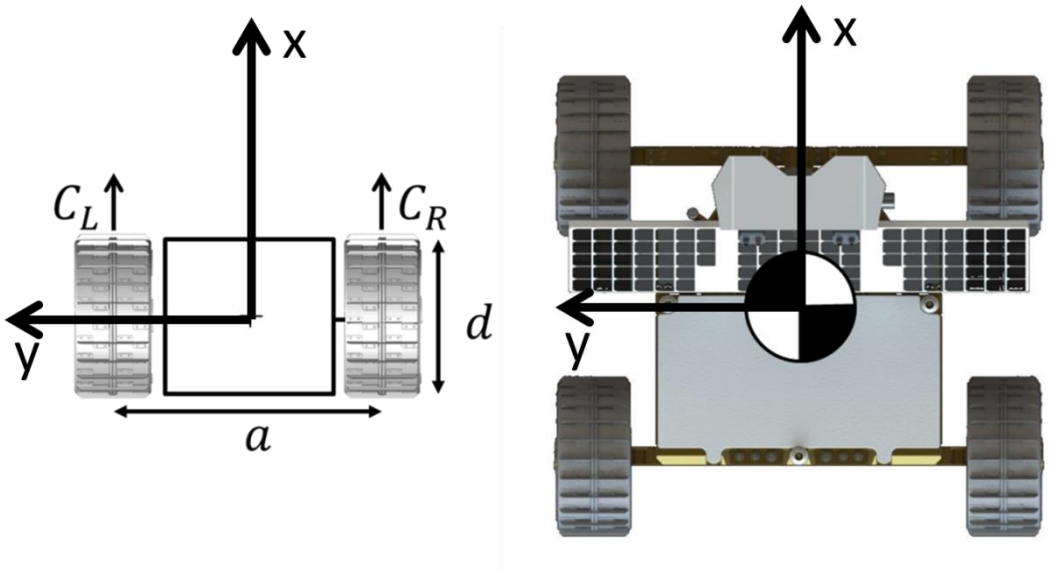

Figure 4: Rover odometry model (left) and actual rover top view (right) with rover coordinate frame

2D Relative Pose Estimation for Differential Drive Vehicle

$$\boldsymbol{S_i = S_{i-1} + \begin{bmatrix}\cos(\theta_i + \varepsilon_{\theta i})\\ \sin(\theta_i + \varepsilon_{\theta i})\end{bmatrix} \frac{C_L + \varepsilon_{C_L} + C_R + \varepsilon_{C_R}}{2}} \quad \textbf{(1)}$$

$S_i = Current\ position\ estimate$
$\theta_i = Current\ absolute\ heading\ estimate\ from\ any\ source\ (rad)$
$\varepsilon_{\theta i} = Error\ in\ current\ absolute\ heading\ estimate\ (rad)$
$C_L = Left\ wheel(s)\ incremental\ travel\ estimate\ (m)$
$C_R = Right\ wheel(s)\ incremental\ travel\ estimate\ (m)$
$\varepsilon_{C_L} = Error\ in\ left\ wheel(s)\ travel\ estimate\ (m)$
$\varepsilon_{C_R} = Error\ in\ right\ wheel(s)\ travel\ estimate\ (m)$

3.2. Absolute Heading: Incremental Estimation

Absolute Heading Estimation from Wheel Odometry

$$\boldsymbol{\theta_i^W = \theta_{i-1}^W + \varepsilon_{\theta_{i-1}^W} + \frac{(c_L+\varepsilon_{c_L})-(c_R+\varepsilon_{c_R})}{a}} \quad \textbf{(2)}$$

$\theta_i^W = Current\ wheel\ odometry\ absolute\ heading\ estimate\ (rad)$
$a = Vehicle\ wheelbase\ (m)$

IMU Integrated Yaw Estimation

$$\vartheta_i^g = \vartheta_{i-1}^g + \boldsymbol{\varepsilon}_{\vartheta_{i-1}^g} + (\dot{\boldsymbol{\vartheta}}_i^g + \boldsymbol{\varepsilon}_{\dot{\vartheta}_i^g})dt \quad \textbf{(3)}$$

$\vartheta_i^g = Current\ \boldsymbol{gyroscope}\ yaw\ estimate$
$\dot{\vartheta}_i^{\boldsymbol{g}} = Current\ \boldsymbol{gyroscope}\ yaw\ rate\ measurement$
$\varepsilon_{\dot{\vartheta}_i^g} = Error\ in\ \boldsymbol{gyroscope}\ yaw\ rate\ measurement$

IMU Roll and Pitch Estimation: Complimentary Filter

$$\beta_i^a = atan2(\ddot{\boldsymbol{y}}_i, \ddot{\boldsymbol{x}}_i)$$

$$\gamma_i^a = atan2\left(-\ddot{\boldsymbol{x}}_i, \sqrt{\ddot{\boldsymbol{y}}_i^2 + \ddot{\boldsymbol{z}}_i^2}\right)$$

$$\beta_{i+1} = \delta(\beta_i + \dot{\boldsymbol{\beta}}_i^g dt) + (1-\delta)\beta_i^a \quad \textbf{(4)}$$

$$\boldsymbol{\gamma_{i+1} = \delta(\gamma_i + \dot{\gamma}_i^g dt) + (1-\delta)\gamma_i^a} \quad \textbf{(5)}$$

$\beta_i = Current\ roll\ estimate$ (rad)
$\gamma_i = Current\ pitch\ estimate$ (rad)
$\delta = Filter\ parameter, \mathbf{0.98}$
$dt = time\ step, \mathbf{0.008}$ (sec)
$\ddot{\boldsymbol{x}}_i = Accelerometer\ gravity\ vector\ measurement\ in\ x\ direction\ (nondim.force)$
$\ddot{\boldsymbol{y}}_i = Accelerometer\ gravity\ vector\ measurement\ in\ y\ direction\ (nondim.force)$
$\ddot{\boldsymbol{z}}_i = Accelerometer\ gravity\ vector\ measurement\ in\ z\ direction\ (nondim.force)$
$\dot{\beta}_i^{\boldsymbol{g}} = Gyroscope\ roll\ rate\ measurement\ (rad/s)$
$\dot{\boldsymbol{\gamma}}_{\boldsymbol{i}}^{\boldsymbol{g}} = Gyroscope\ roll\ rate\ measurement\ (rad/s)$
$\boldsymbol{\beta_i^a} = Accelerometer\ roll\ estimate\ (rad)$
$\gamma_i^{\boldsymbol{a}} = Accelerometer\ pitch\ estimate\ (rad)$

Absolute Heading from IMU Yaw

$$\boldsymbol{\theta_i^{IMU} = atan2(sin(\vartheta_i^g)\cos(\beta_i), \cos(\vartheta_i^g)\cos(\gamma_i) + \sin(\vartheta_i^g)\sin(\gamma_i)\sin(\beta_i))} \quad \textbf{(6)}$$

$\theta_i^{IMU} = Current\ IMU\ heading\ estimate$

3.3. Sun Compass

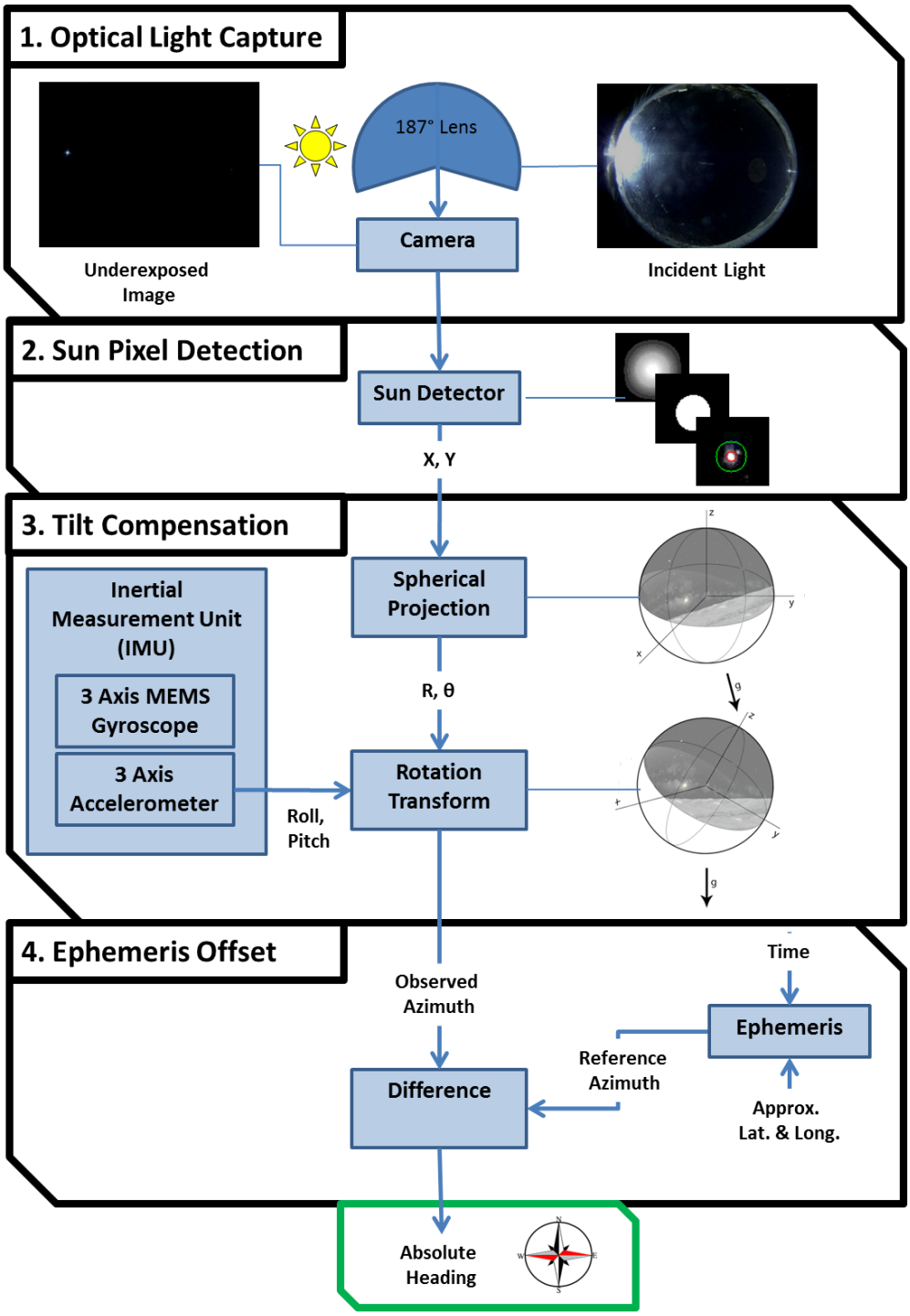

Figure 5: Sun Compass Functional Block Diagram

3.3.1. Optics

The sun compass utilizes an AXIS M3007 IP camera with a 187° fisheye lens. Images were captured once every 1.2 seconds at 800 x 600 pixel resolution. Instead of using solar filters to reduce the level of solar radiation impinging on the camera sensor (as in previous works), this research drastically underexposed the image. This allowed the sun to be tracked while driving continuously over rough terrain without motion blur. Below are two images from the sun compass of the same scene. The left image is with regular exposure and the right image is taken at the exposure setting used in field experimentation. The image at bottom is a composite of all sun images taken during the Lunar Polar Night Test. The artificial sun (commercial light tower) appears higher in the sky (closer to the image center) when the rover is closer to the light tower. The light tower position was accurately surveyed and the proximity effect was corrected using the rover's ground truth position to geometrically calculate a heading offset that was applied to the sun compass' absolute heading.

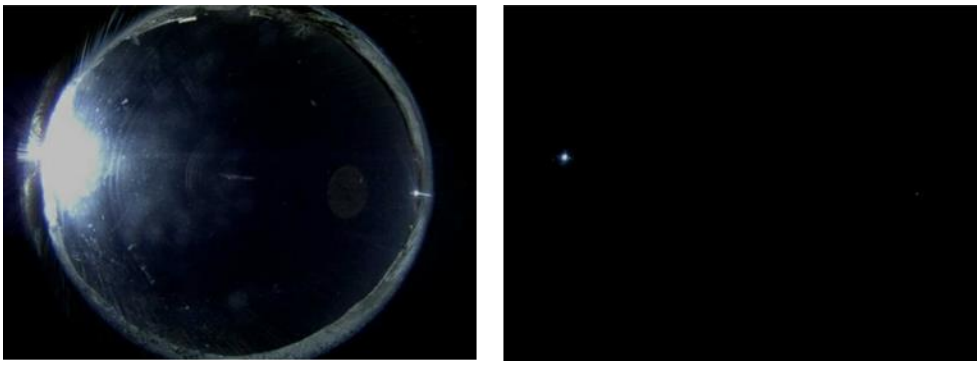

Figure 6: Auto-exposed image (left), underexposed image (right)

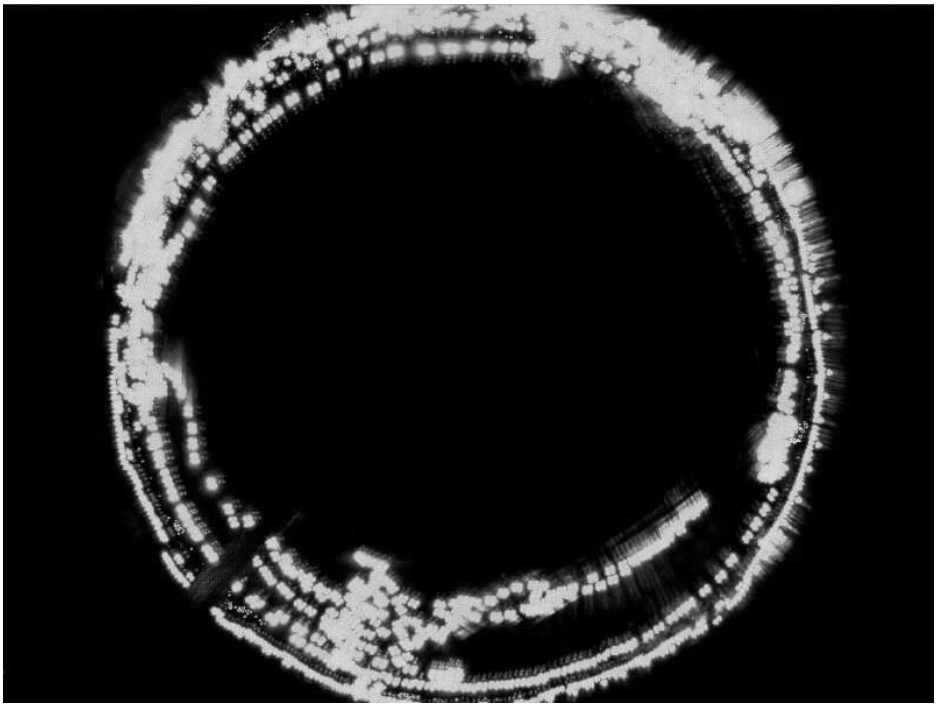

Figure 7: Composite image of all raw sun compass images. Note cropping at image top and bottom due to lens and camera sensor not fully matching, which is common and unavoidable at this sensor size without using a drastically undersized lens (and thus reducing the image circle by at least 1/3)

Figure 8: Example Calibration Test Pattern Image

Resolving heading to objects is only as simple as their location in the image relative to the center when the rover is perfectly flat. An accurate model of light distortion is critical because off axis rover rotations (pitch and roll) cause the sun to move across the image non-radially. Proper lens calibration is necessary in order to correct for the non-uniform distortion of light rays from image center to edge. This was troublesome for many previous researchers, but was resolved with Davide Scaramuzza's omnidirectional camera model and calibration tools which work for lenses up to 195°, which does a 4th degree polynomial fit for the radial distortion of the camera. The following camera parameters were found by using Scaramuzza's OcamCalib software to calibrate the fisheye camera. These parameters define the mapping function from x, y image coordinates to x, y, z unit sphere coordinates. More in depth detail is available in (Scaramuzza et al. 2006). Using unit sphere coordinates makes it possible to correct for rover tilt.

Table 1: 4th order reprojection function polynomial coefficients (ocam_model.ss)

ss(1)	ss(2)	ss(3)	ss(4)	ss(5)
-212.9084213836914	0	0.0014081210740	0.0000007649944	0.0000000036154

Table 2: True Image Center Coordinates

xc	xy
295.4731418087201	399.7080350114414

Table 3:Affine Transformation Parameters

c	1.000529795799015
d	-0.000520933724306710
e	0.0006263747581706951

3.3.2. Detection

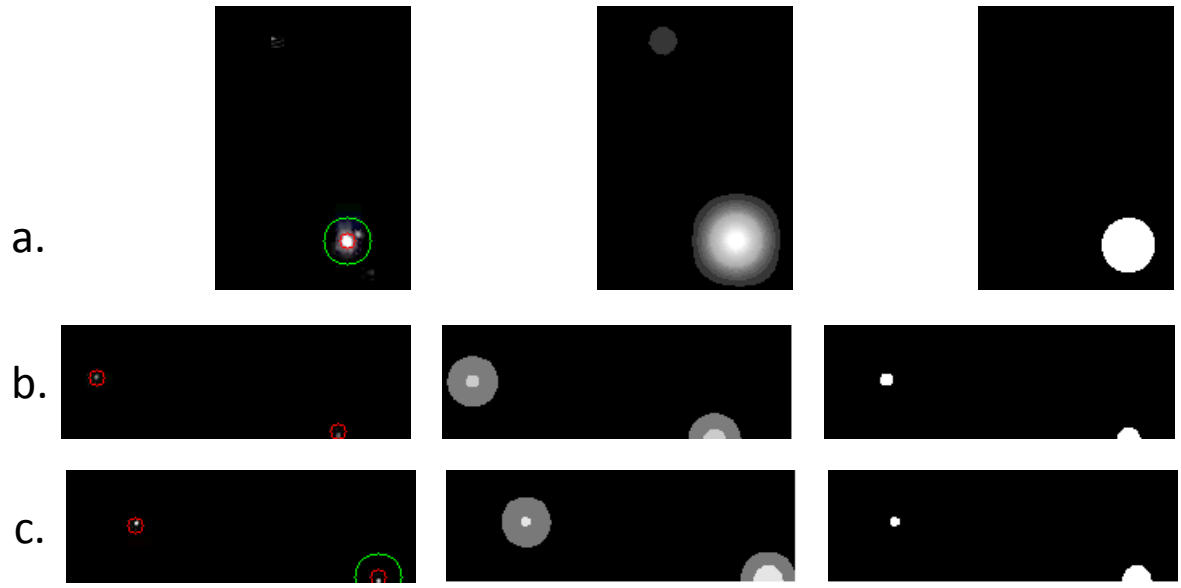

Figure 9: Edge cases for sun detection. [Left] – Auto-exposed image with sun detected (red = candidate, green = accepted); [Middle] – Image after Gaussian blurring (brightness exaggerated for demonstration); [Right] – Binary image created by Otsu thresholding (the outer boundary of each group of white pixels defines the contour used to define a region of interest in the original image).

Detection of the sun spot in the image uses a method that can ignore noise from weaker light sources while still tracking the sun even if it is highly obscured. Weaker light sources are also ignored when the sun is momentarily obscured (by terrain or rover masts). This is accomplished by first applying a Gaussian blur. Otsu thresholding was then performed to create a binary image of light "blobs". OpenCV contour detection was then used to segment these blobs and gather parametric data about each continuous island of white pixels in the image. The largest contour was selected as the sun if it had an area greater than a certain threshold, and had an internal average intensity greater than a predetermined threshold. The internal average intensity of a contour uses the contour boundary to define a region of interest in the original image. The average intensity for the contour becomes the average intensity of all the pixels in the region of interest. This allows the sun to be detected even if it is highly obscured and only a few bright pixels are visible because the average intensity will still be much brighter than similarly shaped lower intensity light sources.

Sun Bearing Estimate in Rover Coordinate Frame

$$\vartheta_r^s = \boldsymbol{atan2}(\boldsymbol{y - v_0, x - u_0}) \quad \textbf{(7)}$$

$\boldsymbol{\vartheta_r^s} = Relative\ to\ sun\ in\ rover\ coordinate\ frame\ (rad)$
$y = Sun\ center\ vertical\ image\ coordinate\ (pixels)$
$x = Sun\ center\ horizontal\ image\ coordinate\ (pixels)$
$v_0 = True\ camera\ vertical\ center\ in\ image\ (pixels)$
$u_0 = True\ camera\ horizontal\ center\ in\ image\ (pixels)$

3.3.3. Tilt

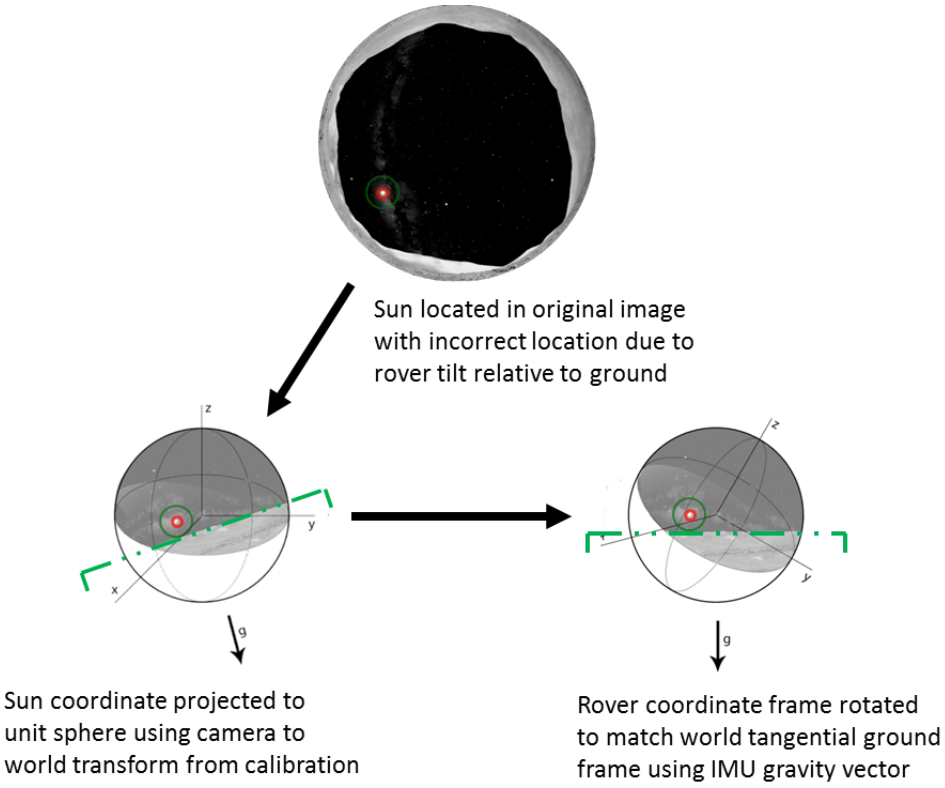

Figure 10: Correcting for a tilted rover orientation using gravity vector from IMU

The naïve results from equation (7) are only valid assuming the rover is on level terrain. This is rarely the case so tilt compensation is always performed using an EPSON V340 6-axis inertial measurement unit to measure the gravity vector. The sun's (x,y) image coordinates are projected onto the unit sphere using Davide Scaramuzza's projection function that is defined by the intrinsic lens parameters determined in the previously mentioned camera calibration. This creates the relative 3D vector to the sun in the robot coordinate frame. The robot coordinate frame is then rotated by the gravity vector to match the global coordinate frame that is tangent to the surface of the celestial body. This is done by creating a rotational transformation matrix that represents the negative of the rover's roll and pitch angles ($-\beta \; and \; -\gamma$, respectively), and applying it to the rover's coordinate frame.

Sun Bearing Estimate in Global Coordinate Frame

$$\overline{rover\_2\_sun} = f(\mathrm{x}, \mathrm{y}, \mathrm{xc}, \mathrm{yc}, \mathrm{c}, \mathrm{d}, \mathrm{e}, \mathrm{ss})$$
$$M = f(\beta, \gamma)$$
$$\boldsymbol{\theta_r^s = cartesian\_2\_spherical}(\boldsymbol{M} * \overline{\boldsymbol{rover\_2\_sun}}) \quad \textbf{(8)}$$

$M = 3D\ rotation\ matrix\ encoding\ roll\ and\ pitch$
$\overline{rover\_2\_sun} = 3D\ vector\ from\ rover\ to\ sun\ in\ rover\ coordinate\ frame$
$\theta_r^s =$ Relative bearing to sun in global coordinate frame

The sun compass was mounted to a custom built 3-axis gimbal (shown below) and tracked a light source representing an artificial sun. This setup was used to verify that for a fixed yaw and various arbitrary rolls and pitches, the compass' heading remained constant. Further testing was also performed to ensure that the compass' heading and gimbal's azimuth properly corresponded even for severe rolls and pitches. Throughout these tests, compass heading error of less than 0.5° was common, increasing up to 2° only rarely at extreme angles > 30°.

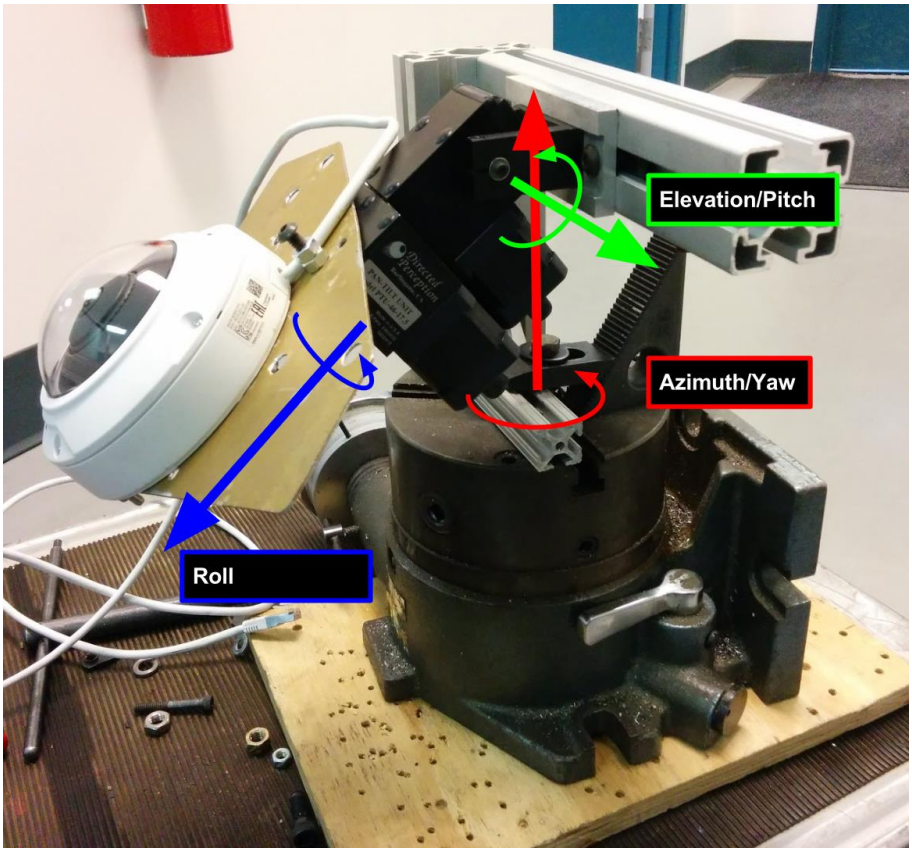

Figure 11: 3 axis gimbal with camera and IMU for calibration and testing. Azimuth/yaw axis is set and measured by a precision machinist's turntable

3.3.4. Ephemeris

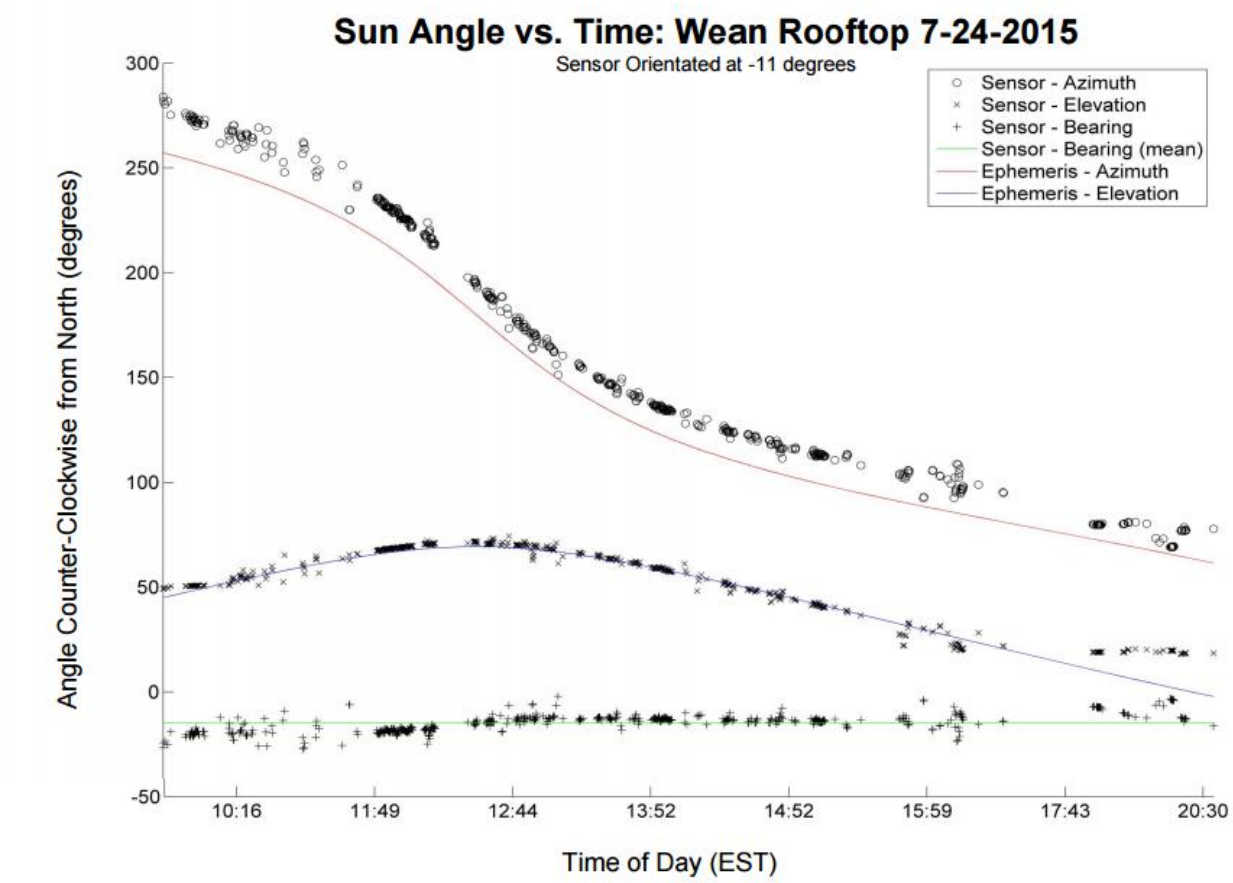

Figure 12: Stationary sun compass test results for 1 day, using ephemeris

To show operability with the real sun and ephemeris, the sun compass observed roughly 11 hours of solar transit on July 24, 2015 while stationary at a known heading of -11°. Note the occasional outliers during the day that are caused by cloud interference. The more prominent groups of outliers occur near dawn and sunset and are caused by trees and buildings occluding the sun near horizon. These inconsistencies were overcome by field testing on the rover at night with a controlled light source as an artificial sun. The ephemeris was not used in the night field test, but was shown to work effectively in concert with the sun compass.

4. Lunar Polar Analog Field Experiment

Figure 13: View from rover's forward facing navigation camera during traverse

An innovation of this research is utilization of an artificial sun during night testing. This overcomes the problems and errors introduced by clouds and atmospheric curvature during all previous experiments navigating rovers with a sun compass. Despite best prior attempts for sun detection algorithms, no sun compass has achieved fast, reliable, and accurate operation without this experimental advantage.

The rover was driven lengthwise down a large artificial trench dug at a slag processing facility. A commercial construction light tower was used as an artificial sun. The trench gently slopes away from the direction of the light tower and drops roughly 4m over a span of 150m. The trench is 30m wide at its narrowest point and the trench floor is made of a hard packed dirt and rock mixture on either sides of a ~50m 'island' of coarse sand. Most loose rocks range from 5cm to 1cm in diameter with occasional rocks larger than 20cm in diameter. Many small hills, ridges, and uneven surfaces populate the trench floor.

Figure 14: Light tower used as the artificial sun

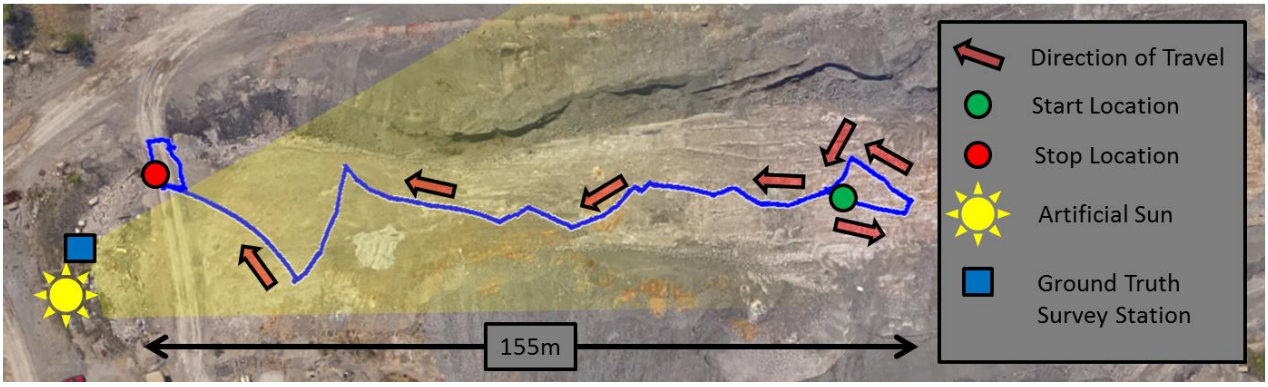

Figure 15: Map of Lunar Polar Analog Field Experiment and 302m Traverse

The sun compass was tested on a teleoperated rover in a simulated lunar environment on November 15, 2005. The test was performed just after sunset and used an artificial light source supported roughly 10m above the driving surface. The four-wheel differential drive engineering prototype lunar rover Andy was used as a test platform. The drive lasted roughly two hours and covered about 350m of ground, of which 302m is used for analysis. The rover's ground truth position was tracked at around 10Hz by a robotic total survey station to millimeter precision. The survey station laser targeted and tracked a corner cube mirror prism attached to the top of the rover's camera mast.

4.1. Rover

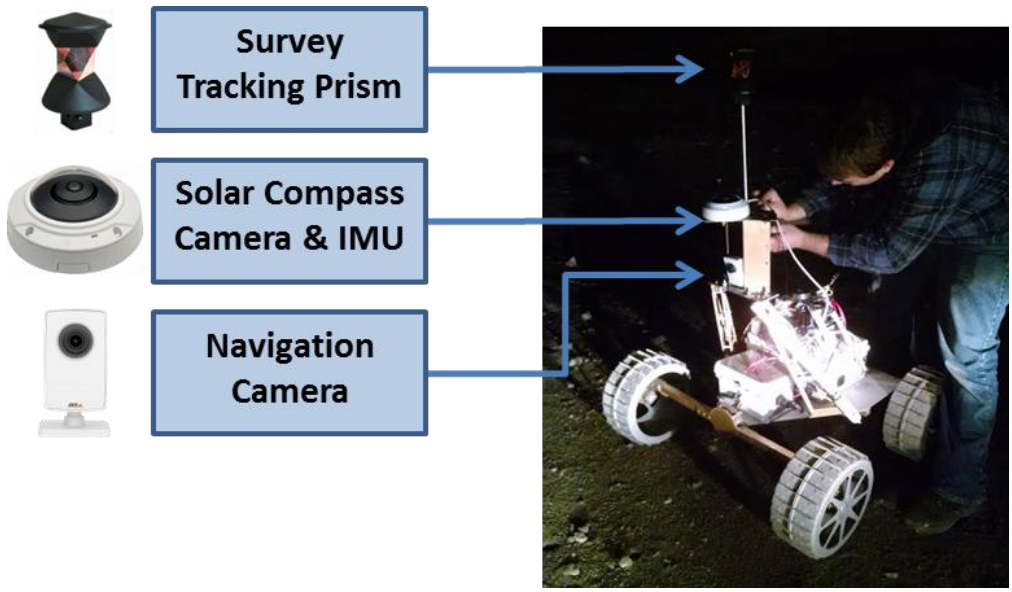

Figure 16: Andy Engineering rover testbed being prepared for the sun compass field experiment

Andy has been used for several kilometers of field testing in lunar-like environments and won the Google Lunar X-Prize Milestone Prize for mobility. It has a passive front rocker suspension, a low center of gravity, and high belly clearance. It can drive up a 32.5° slope and has a 45° tip-over angle. An Intel Nuc computer was onboard the rover and served as the visual processor for the sun sensor, as well as a data logger for the IMU and sun compass image data. A Texas Instruments Hercules embedded microcontroller commanded Andy's lower level driving functions, and received driver commands over a direct serial radio link to the ground station. Rover to ground station communications are both over a long

range Wi-Fi connection and omnidirectional serial radio. The ground station consists of a server hosting a web interface for the drivers and acts as a data logger for internal rover information such as wheel turns and driver commands. Andy also is equipped with hot swappable auxiliary batteries that allow for extended continuous operation for greater than 8 hours.

Figure 17: Andy with decorative solar panel simulator (left), Andy maintained a correct sun heading in extreme near tip over stance (right)

5. Results

Sun compass operation at night with an artificial sun allowed the full potential of the sun compass to be demonstrated with reliability and frequency that far surpasses previous efforts in the literature. This made it possible for the first time to achieve accurate route determination using the high rate 187° field of view sun compass as the exclusive source of heading. This research is also novel in that night field test with an artificial sun is the first representation of the performance of a continuous and automatic sun compass on the moon (and other celestial bodies that have no clouds to block the sun).

Using high rate sun compass heading, relatively low accuracy wheel odometry distance and without the benefit of Kalman filtering and visual odometry, this configuration achieved a route determination with a 4.6% position error after 302m of travel. This error is percent of distance traveled at the location in the path of the maximum position error. This is remarkable in that it achieves less error than the 6% mean error for 300m route determinations found by Lambert (2010) who used a narrower field of view space grade continuous sun sensor tightly integrated with binocular visual odometry. Additionally, this is an improvement over the mean route determination errors of 9.6% at 35m and 6.2% at 45m reported by Huntsberger et al. (2002) when using and Extended Kalman Filter to fuse end point sun sensor data, wheel odometry, and gyroscopic heading on an actively steered six wheeled rover.

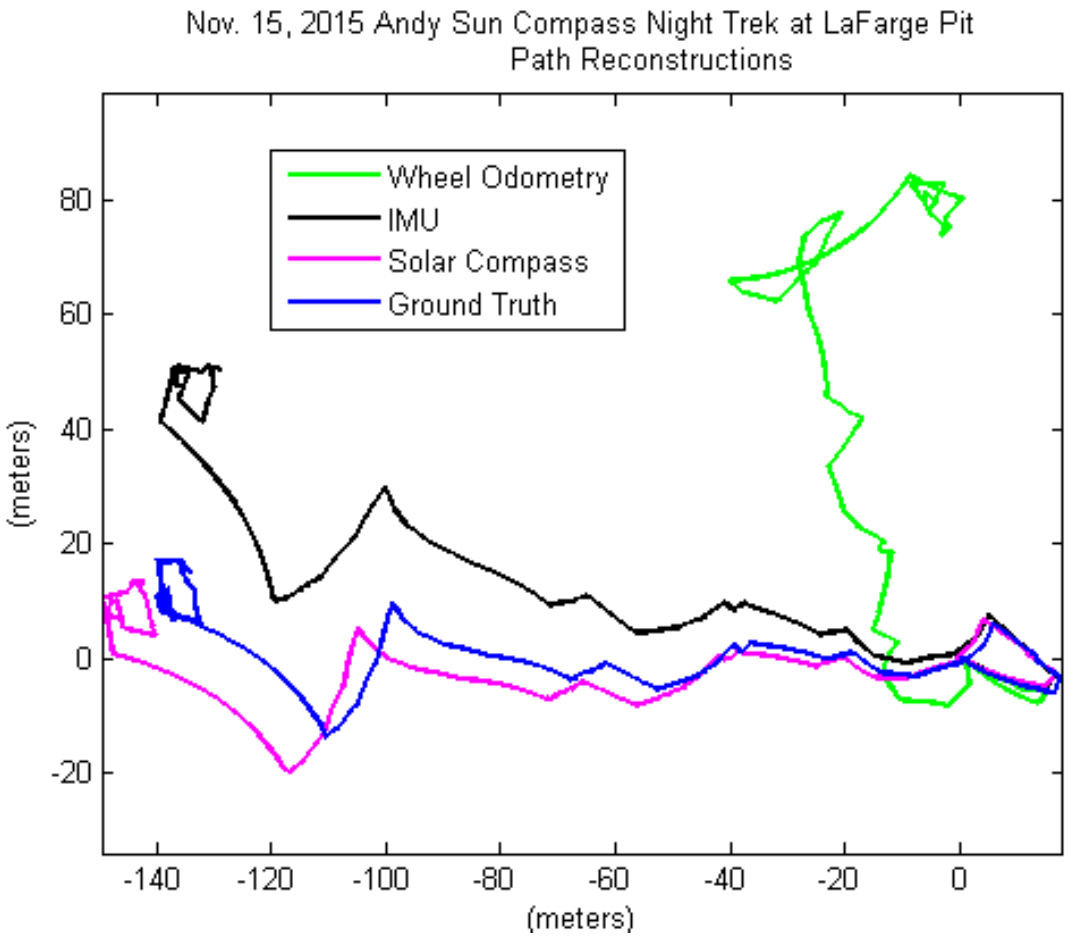

Figure 18: Route determinations overlaid onto ground truth path for night experiment

Three reconstructed paths and the ground truth path are shown in Figure 18 above. The three reconstructed paths – green, black, and purple – were created using Equation (2). All plots in this document follow the same color scheme as outlined in the table below.

Table 4: Route Determination Legend

Label	Plot Color	Distance Source	Heading Source
Wheel Odometry (WO)	**Green**	Incremental from wheel odometry and equation (1)	wheel odometry and equation (2)
Inertial Measurement Unit (IMU)	**Black**	Incremental from wheel odometry and equation (1)	Integrated heading gyro and equation (6)
Sun Compass	**Purple**	Incremental from wheel odometry and equation (1)	Absolute heading from sun equation (8)
Ground Truth	**Blue**	Absolute position from laser tracking survey station	Numerical differentiation

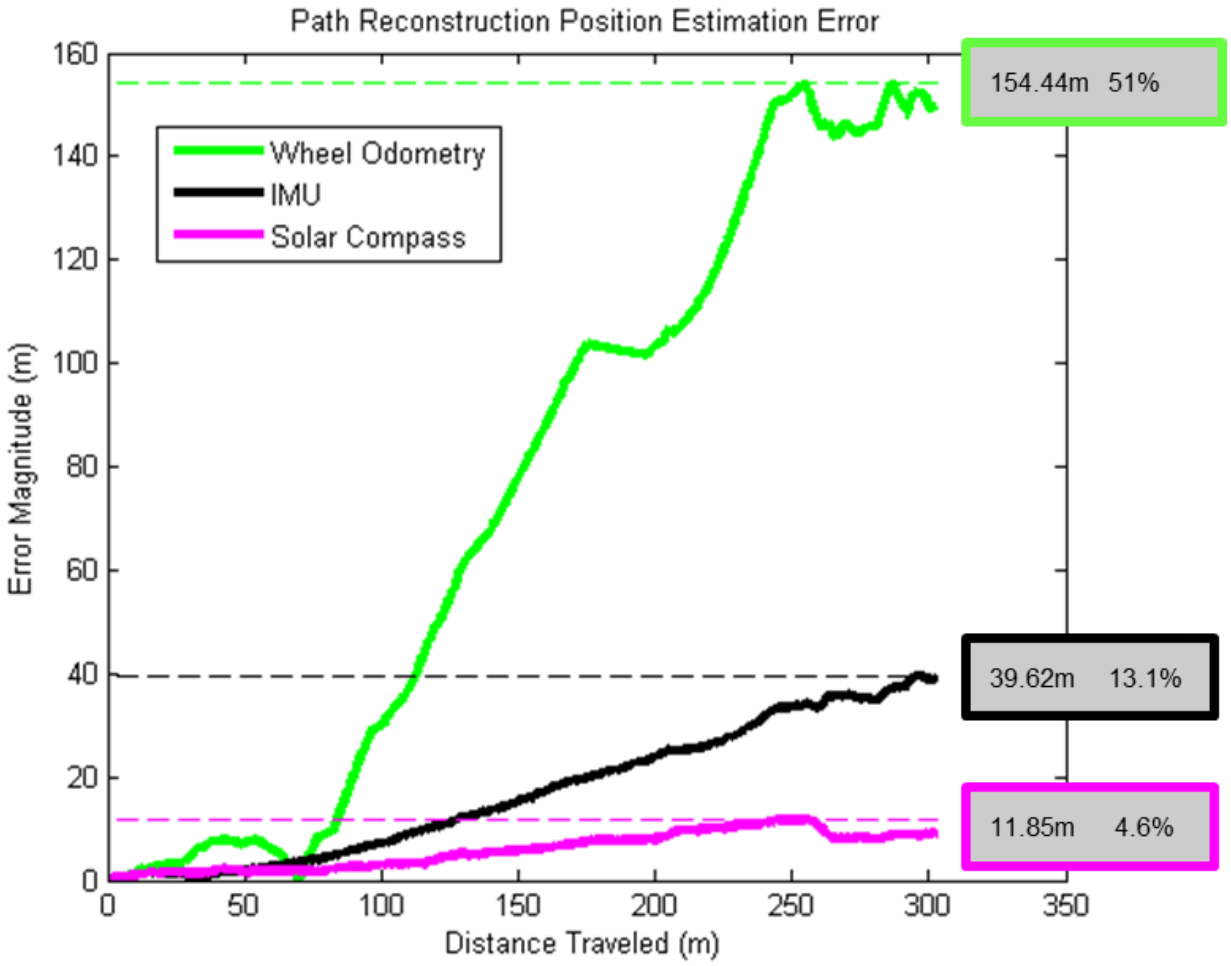

Figure 19: Position error of the three route determinations vs. ground truth. Maximum error along path is indicated with the dashed line and gray boxed numbers. Error percentage is percent of total distance traveled at the time of that error.

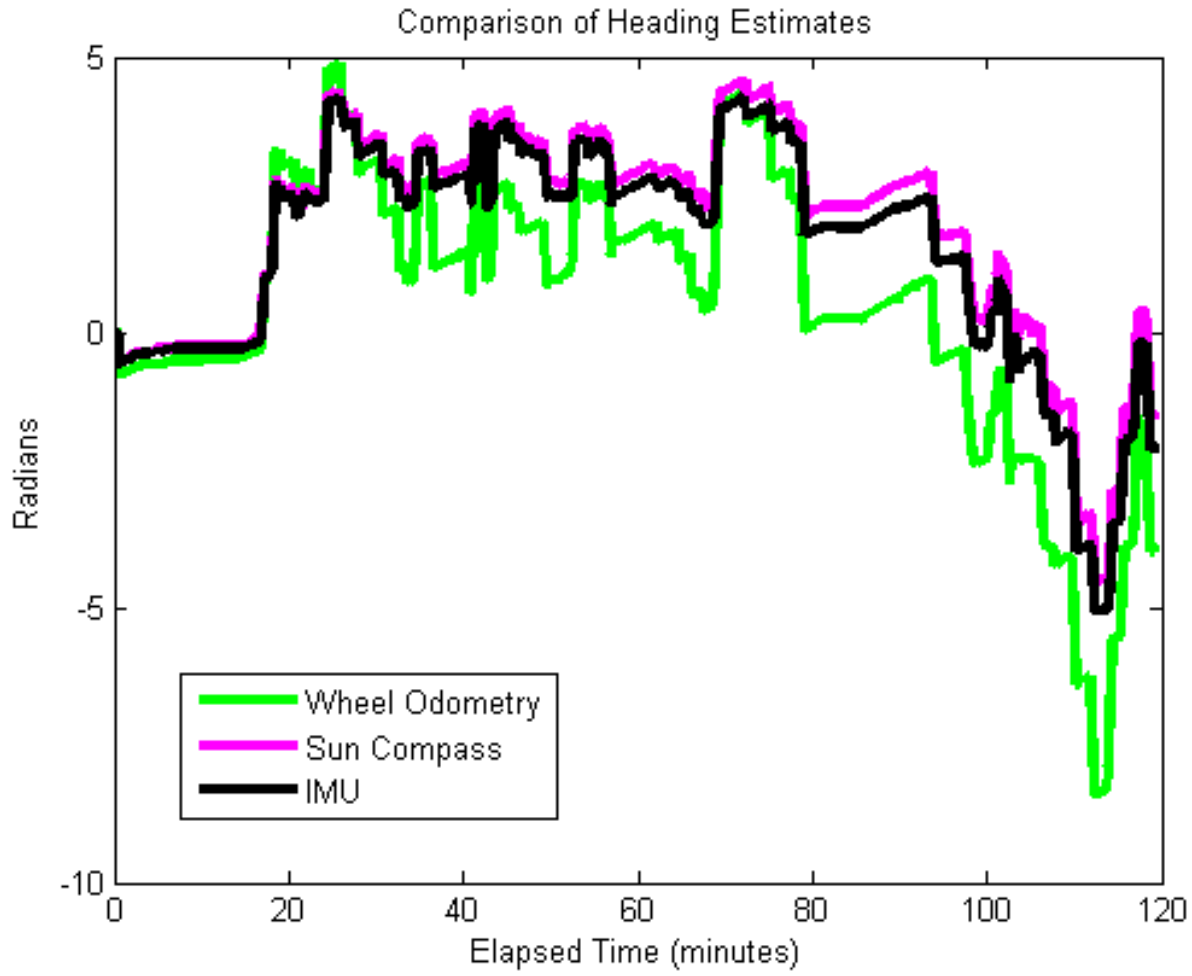

Figure 20: Comparison of the three heading estimates. Notice the gradual deviation of the IMU heading from the sun compass heading

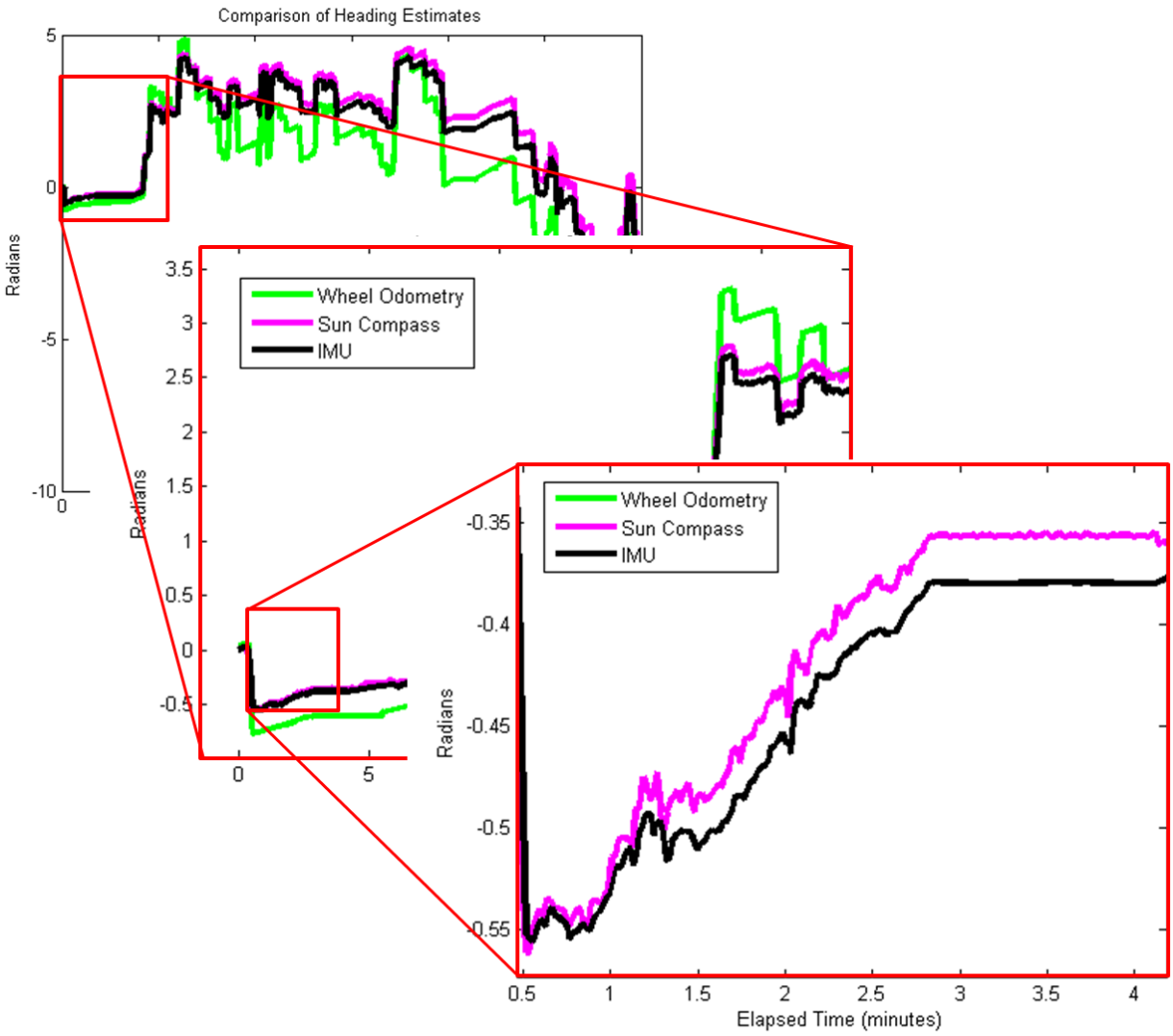

Figure 21: Detail heading comparison at beginning of trek showing initial close agreement between sun compass and IMU

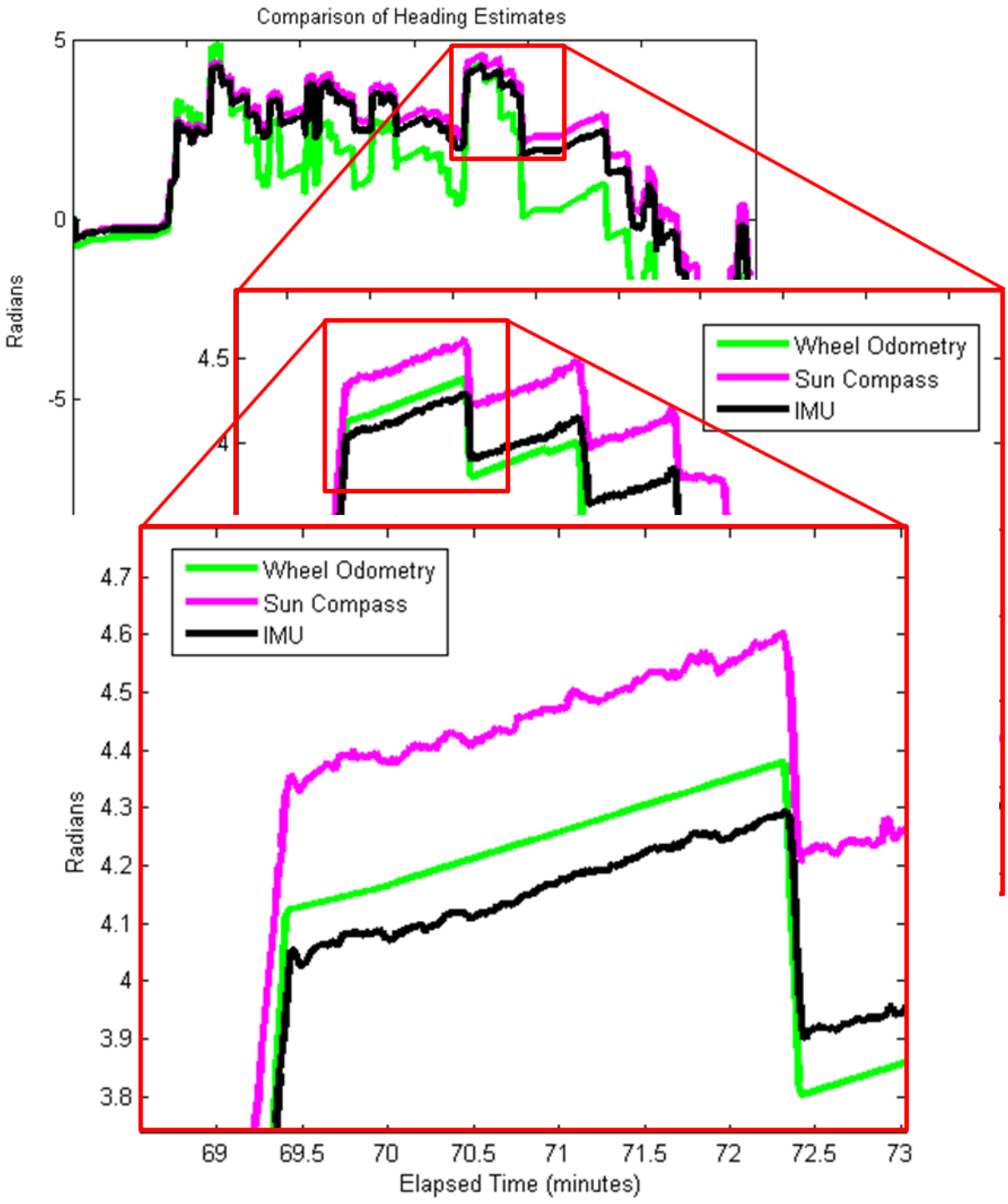

Figure 22: Detail of heading comparison showing divergence of sun compass and IMU heading after roughly 200m of the trek. Relative change in heading remains in close agreement between the two measurements.

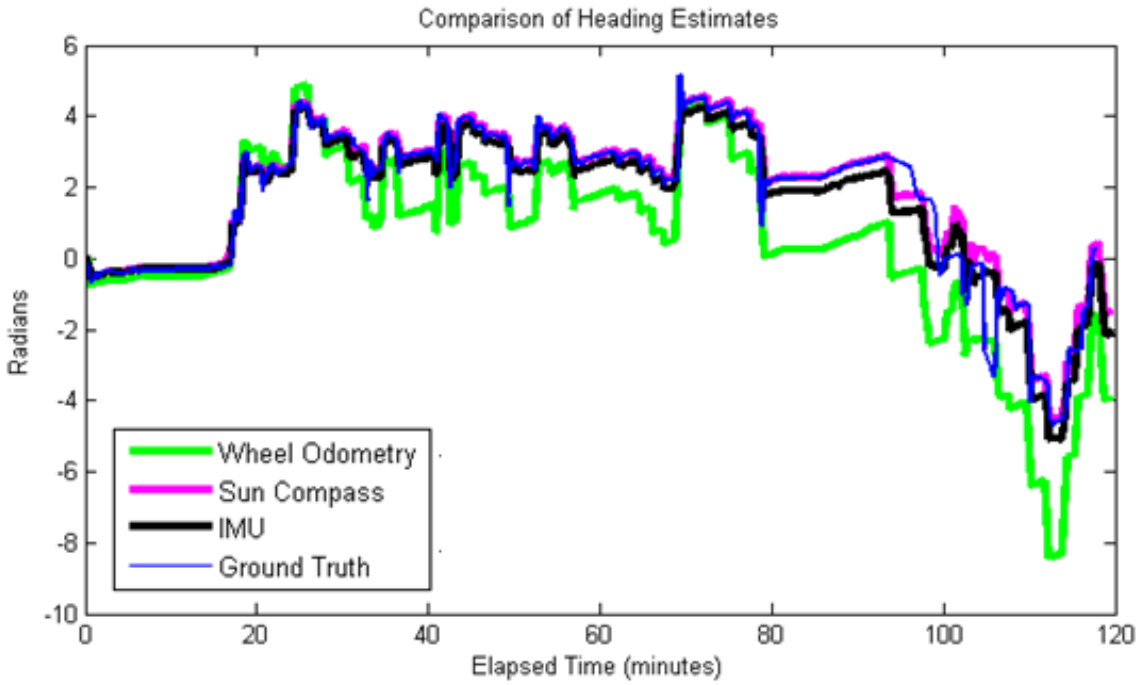

Figure 23: Comparison of ground truth to heading estimates. Note close overlay of Blue on purple. Also note errors in ground truth heading around 100 minutes due to excessive noise.

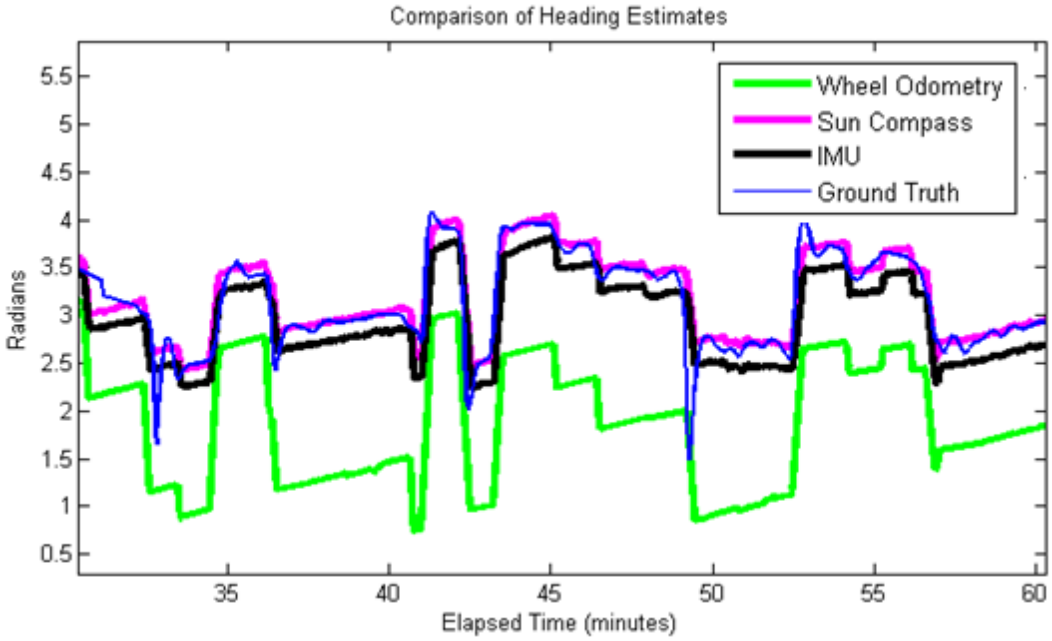

Figure 24: Filtered ground truth heading approximation closely follows the sun compass heading.

The noise recorded in the ground truth position data required heavy filtering before it was suitable for generating a ground truth heading for sensor comparisons. The comparison shows close agreement between ground truth heading and the sun sensor.

Ground truth position data was first subsampled with a 1:25 ratio and then further reduced by removing each data point that did not move more than 0.04m from the previous point. The reduced position data was then smoothed using a 4th order Butterworth filter. The heading at each point was calculated using the arctangent of the line segment joining that point to the next point. Figure 23 and Figure 24 on the previous page show the filtered ground truth heading data. Figure 25 below shows a detail view of the unfiltered ground truth heading data.

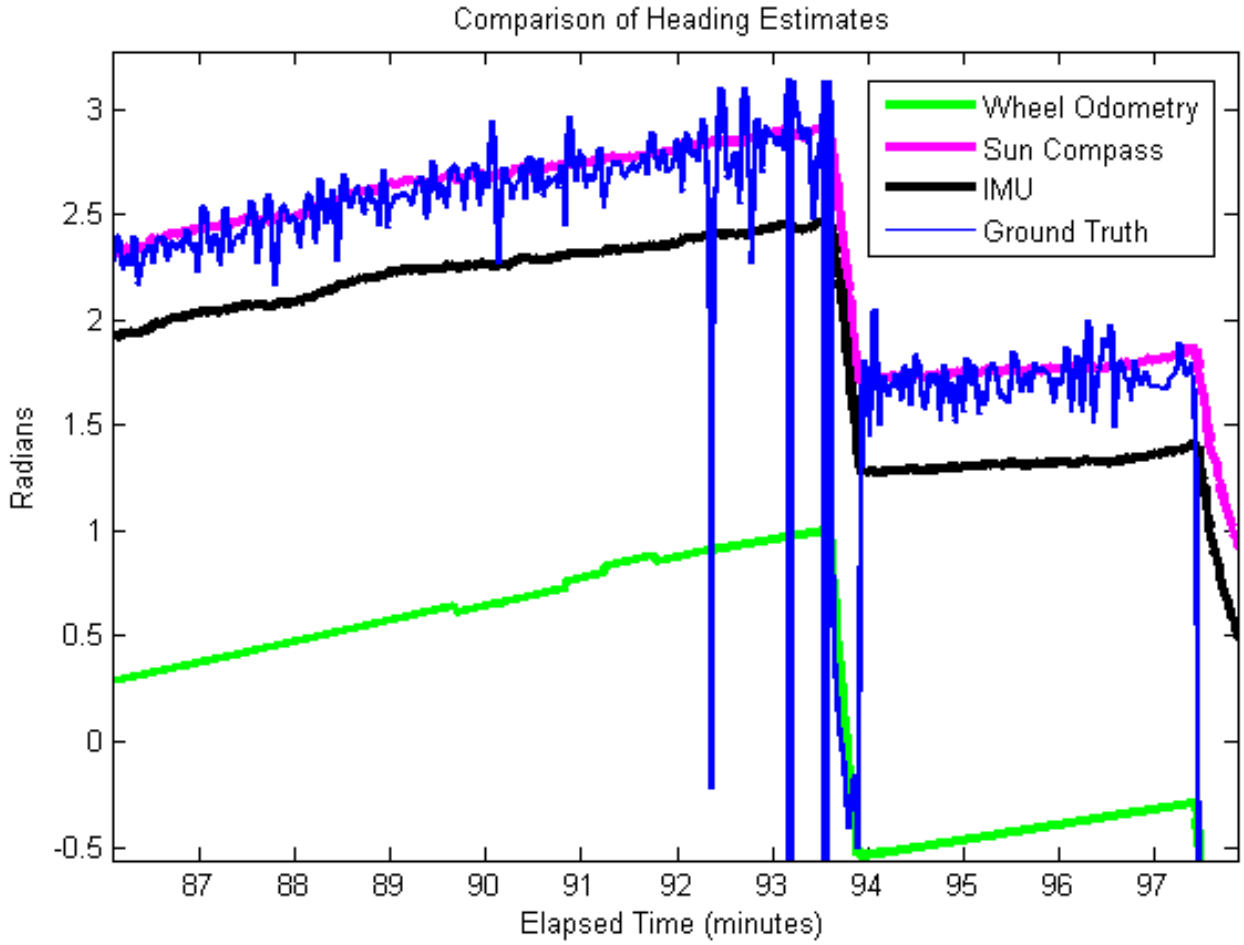

Figure 25: Ground truth heading first order approximation without filtering shows excessively noise.

6. Conclusions and Future Work

A high rate sun compass was shown to reduce localization error even when compared to state of the art methods such as visual odometry, inertial navigation, and sensor fusion. This was experimentally proven with the route reconstruction results of a novel controlled lighting field test at night in lunar like conditions. This test was to the author's knowledge the first of its kind and allowed a newly developed novel sun compass to perform as a reliable primary, and even exclusive source of heading. This is in stark contrast to previous research where the sun compass' role was merely to augment other sensors. Sun compass heading is absolute, does not drift, and its advantages increase with increasing driving distance and duration. Route determination utilizing a high rate sun compass and wheel odometry matches prior results that fused both visual odometry and sun compass heading.

The presence of clouds confounds terrestrial testing of any sun compass, and has limited its prior use to secondary measurement. Modern advances have overcome many of the early problems with sun compassing, mainly field of view, calibration, and tilt compensation. Additionally, the night test shows that the sun compass is exceptionally well suited for robotic exploration of the moon, particularly the polar regions.

Despite the very wide angle lens used in this research, the sun compass could still benefit greatly from a less restricted field of view. Developing innovative optics to achieve a full-sphere field of view could allow the sun compass and navigation camera to be one in the same and offer immense advantages to both. Another powerful development opportunity is to miniaturize the presented sun compass, which is made from all commercial off the shelf parts. There exists a great opportunity to reduce size, increase reliability, and to take on other development actions to make this sun compass relevant for space use.

Given the significant results achieved in this single field test, a testing campaign should be enacted to achieve statistical significance of the sun compass' effect on route determination error. Concurrently, there is much room for modeling, testing, calibrating, and optimizing of this sun compass to nullify and characterize its uncertainty. The prospects abound for utilizing a high rate wide field of view sun compass to empower robotic exploration. Even after millennia, determining absolute heading from the sun is still a powerful tool for exploration, and may once again enable great discoveries.

7. Bibliography

Ali, K.S. et al., 2005. Attitude and Position Estimation on the Mars Exploration. *IEEE Conference on Systems, Man, and Cybernetics*.

Bapna, D. et al., 1998. The Atacama Desert Trek: outcomes. *Proceedings. 1998 IEEE International Conference on Robotics and Automation (Cat. No.98CH36146)*, 1(May).

Baumgartner, E.T. et al., 2001. Rover Localization Results for the FIDO Rover. *Spie*, 4571, pp.34–44.

Betke, M. & Gurvits, L., 1997. Mobile robot localization using landmarks. *IEEE Transactions on Robotics and Automation*, 13(2), pp.251–263.

Borenstein, J. et al., 1997. Mobile robot positioning: Sensors and techniques. *Journal of Robotic Systems*, 14(4), pp.231–249. Available at: http://doi.wiley.com/10.1002/(SICI)1097-4563(199704)14:4<231::AID-ROB2>3.3.CO;2-1.

Borenstein, J., Everett, H.R. & Feng, L., 1996. Where am I? Sensors and methods for mobile robot positioning. *University of Michigan*, 119, p.120.

Borenstein, J. & Feng, L., 1996. Gyrodometry: A New Method for Combining Data from Gyros and Odometry in Mobile Robots. *IEEE International Conference on Robotics and Automation*, pp.423–428.

Cozman, F. & Krotkov, E., 1995. Robot Localization using a Computer Vision Sextant. *IEEE International Conference on Robotics and Automation*, pp.106–111.

Eisenman, A.R., Liebe, C.C. & Perez, R., 2002. Sun sensing on the Mars exploration rovers. *IEEE Aerospace Conference*, 5(818), pp.2249–2262.

Huntsberger, T. et al., 2002. Rover autonomy for long range navigation and science data acquisition on planetary surfaces. *Robotics and Automation, 2002. Proceedings. ICRA '02. IEEE International Conference on*, 3(May), pp.3161–3168.

Jones, E.M., 1996. Stand-Up EVA. Available at: http://www.hq.nasa.gov/alsj/a15/a15.html.

Lambert, A.J., 2010. Visual Odometry Aided by a Sun Sensor and an Inclinometer. *Engineering*.

Lamon, P., 2008. *3D-Position Tracking and Control for All-Terrain Robots*, Berlin Heidelberg: Springer-Verlag.

Li, R. et al., 2006. Spirit rover localization and topographic mapping at the landing site of Gusev crater, Mars. *Journal of Geophysical Research E: Planets*, 111, pp.1–13.

Li, R.X. et al., 2005. Initial results of rover localization and topographic mapping for the 2003 mars exploration rover mission. *Photogrammetric Engineering and Remote Sensing*, 71(10), pp.1129–1142.

Maimone, M., Cheng, Y. & Matthies, L., 2007. Two years of visual odometry on the Mars Exploration Rovers. *Journal of Field Robotics*, 24(3), pp.169–186.

Scaramuzza, D. et al., 2006. A Toolbox for Easily Calibrating Omnidirectional Cameras. *IROS*.

Sheshadri, A. et al., 2012. Position estimation by registration to planetary terrain. *IEEE International Conference on Multisensor Fusion and Integration for Intelligent Systems*, 78701, pp.432–438.

Thrun, S., 2002. Probabilistic robotics. *Communications of the ACM*, 45(3), pp.1999–2000.

Trebi-Ollennu, A. et al., 2001. Design and analysis of a sun sensor for planetary rover absolute heading detection. *IEEE Transactions on Robotics and Automation*, 17(6), pp.939–947.

United_States_Department_of_the_Interior, 1973. *Manual of Instructions for the Survey of the Public Lands of the United States*,

Volpe, R., 1999. Mars rover navigation results using sun sensor heading determination. *Proceedings 1999 IEEE/RSJ International Conference on Intelligent Robots and Systems. Human and Environment Friendly Robots with High Intelligence and Emotional Quotients (Cat. No.99CH36289)*, 1, pp.460–467. Available at: http://ieeexplore.ieee.org/lpdocs/epic03/wrapper.htm?arnumber=813047.